

Deep Learning for Waveform Estimation and Imaging in Passive Radar

Bariscan Yonel[†], Eric Mason^{*}, and Birsen Yazici[†]

[†]Department of Electrical, Computer and System Engineering, Rensselaer Polytechnic Institute, Troy, NY 12180 USA

^{*}Tactical Electronic Warfare Division, Naval Research Laboratory, Washington, DC 20375, USA

Abstract

We consider a bistatic configuration with a stationary transmitter transmitting unknown waveforms of opportunity and a moving receiver and present a Deep Learning (DL) framework for passive synthetic aperture radar (SAR) imaging.

Existing passive radar methods require two or more antennas which are either spatially separated or colocated with sufficient directivity to estimate the underlying waveform prior to imaging. Our approach to passive radar only requires a single receiver, hence reduces cost and increases versatility. We approach DL from an optimization perspective and formulate image reconstruction as a machine learning task. By unfolding the iterations of a proximal gradient descent algorithm, we construct a deep recurrent neural network (RNN) that is parameterized by transmitted waveforms. We cascade the RNN structure with a decoder stage to form a recurrent-auto encoder architecture. We then utilize backpropagation to learn transmitted waveforms by training the network in an unsupervised manner using SAR measurements. The highly non-convex problem of backpropagation is guided to a feasible solution over the parameter space by initializing the network with the known components of the SAR forward model. Moreover, prior information regarding the waveform structure is incorporated during initialization and backpropagation. We demonstrate the effectiveness of the DL-based approach through extensive numerical simulations that show focused, high contrast imagery using a single receiver antenna at realistic SNR levels.

1 Introduction

1.1 Motivations

Deep Learning (DL) has propelled significant developments in wide range of applications in science and engineering [1]. These include advancements in medical imaging [2, 3], computer vision [4, 5], artificial intelligence [6], with impressive performances in object recognition, natural language processing, and many other applications [1, 7].

Currently, most prominent applications of DL involve establishing complex decision boundaries in high dimensional parameter spaces using large amounts of training data. We instead consider DL as a joint estimation framework for problems that contain unknown parameters in the measurement model. Passive radar imaging falls into such class of problems, in which transmitter locations or transmitted waveforms may not be known a priori.

Passive radar has been an area of intense research due to proliferation of transmitters of opportunity and several advantages it offers. These include efficient use of electromagnetic spectrum, increased stealth, reduced cost among others [8–18]. Existing passive radar methods require two or more antennas, either spatially separated or colocated with sufficient directivity and gain. Specifically, these methods rely on correlating pairs of measurements acquired by two different antennas. These methods can be classified into two major categories: passive coherent localization (PCL) [19–23] and time-(or frequency) difference-of-arrival (TDOA/FDOA) backprojection [8, 17, 24–32].

The PCL approach attempts to recover a copy of the transmitted waveform by filtering the received signal acquired by an antenna directed to a transmitter of opportunity. This is followed by matched filtering

of the received signal acquired by another antenna directed to a scene of interest [33–36]. This approach relies on accurate estimation of transmitted waveforms. Recently, several algorithmic advances have been reported in waveform estimation using the structure of Digital Video Broadcasting-Terrestrial (DVB-T) signals as illuminators of opportunity [37–41]. In addition to two antennas at each receiver location, and priori knowledge on the signal structure, PCL also requires direct line-of-sight to a transmitter of opportunity and high signal to noise ratio (SNR) for the received signal from the transmitter.

In the TDOA/FDOA approach, received signals acquired by two or more sufficiently far-apart receivers are correlated and backprojected based on time or frequency difference of arrival to form an image of a scene [8, 24–30]. As compared to PCL, TDOA/FDOA technique does not require direct-line-of-sight to a transmitter, high SNR, or the knowledge of transmitter location. However, the method is limited to imaging widely separated point scatterers. To overcome this limitation, an alternative method based on low-rank matrix recovery (LRMR) has been developed [18]. Despite its effectiveness in reconstructing scenes with extended targets, LRMR-based approach has significant computational and memory requirements, which preclude its applicability to realistically sized images.

Recently, DL framework has been investigated for signal processing problems. Specifically, with an emphasis on sparse coding and compressed sensing. In [42], the iterative soft thresholding (ISTA) and coordinate descent algorithms were implemented via a recurrent neural network (RNN), in which each layer of the network corresponded to an iteration. The model was trained in a supervised manner using the desired solutions for sparse codes of the corresponding inputs with the goal of accelerating convergence. This fundamental observation was exploited to implement an approximate message passing algorithm [43], to learn problem specific gradient descent parameters [44], and to estimate parametrized priors [45]. In [46] we extended the idea of emulating iterative maps using RNNs to image reconstruction problems in Bayesian framework. We considered the passive imaging problem in which the transmitter location is unknown, and used DL to refine the phase component of the synthetic aperture radar (SAR) forward model. Training was done in an unsupervised manner using SAR received signal directly via complex backpropagation [47]. The method produces focused imagery without increasing the computational complexity of the proximal gradient descent algorithm which its based on.

1.2 Our Approach and Its Advantages

In this paper, we develop a DL-based approach for passive SAR image reconstruction when the transmitted waveforms of opportunity are unknown. Specifically we present a deep network architecture and an unsupervised training scheme to learn transmitted waveforms as a parameter of the SAR imaging problem, while reconstructing focused imagery. The key advantage of our approach as compared to other methods is that it only requires a single receiver antenna, thereby providing reduced cost and increased versatility. We extend our preliminary studies on the joint waveform estimation and imaging problem in [48, 49], develop the theory and demonstrate its effectiveness in extensive numerical simulations.

We assume a stationary transmitter transmitting unknown waveforms and a moving receiver collecting backscattered signal from a scene of interest. We further assume that the structural form of transmitted waveforms are known and represent them as a linear combination of known basis functions. A wide range of communication and broadcasting waveforms falls into such class of waveforms including DVB-T and WiMAX signals.

Following our approach in [46, 50], we take an optimization perspective to DL, and interpret image reconstruction as a machine learning task. We derive a proximal gradient descent update to solve for scene reflectivity, and formulate a recurrent-auto encoder that is parameterized by unknown waveform coefficients. We utilize complex backpropagation to derive the parameter update equations, making our method applicable to both real and complex waveforms. We then utilize backpropagation to learn transmitted waveforms by training the network in an unsupervised manner using SAR measurements. The highly non-convex problem of backpropagation is guided to a feasible solution over the parameter space by initializing the network with the known components of the SAR forward model. Moreover, prior information regarding the waveform structure is incorporated during initialization and backpropagation.

Unlike PCL, our approach does not require an antenna directed to a transmitter of opportunity, or a specific structure on the transmitted signal. Instead, it provides a method to incorporate any prior information of the waveform structure to improve waveform estimation and imaging. We formulate our

method for transmitted signals with a flat spectrum, and utilize it as a constraint for waveform estimation. This formulation is applicable to illuminators of opportunity generated from a wide range of spread spectrum methods such as frequency phase shift keying (PSK) modulated, code division multiplexed (CDM) and orthogonal frequency division multiplexed (OFDM) signals. However, such prior knowledge is used merely as a constraint in waveform estimation, and lack thereof is not a limiting factor for the method.

Our method is based on unsupervised training, in that, it does not require SAR images, but SAR received signal in training. As a result, we avoid upper bounding the quality of reconstructed images by SAR images reconstructed using conventional methods.

Finally, in addition to the benefits of deploying a single receiver, our method provides means of estimating the waveform with the task of reconstructing enhanced imagery. This is achieved by formulating waveform estimation as minimization of the mismatch between received SAR signal and the synthesized SAR signal from the reconstructed scene. We show that our DL approach produces high contrast imagery when trained under realistic SNR levels. Our results indicate that the performance is strongly correlated to the accuracy of the estimated flat spectrum waveform, which demonstrates the joint estimation capability of the DL-approach.

1.3 Organization of the Paper

The rest of the paper is organized as follows. In Section 2, we introduce background material on deep learning. In Section 3, we present the received signal and waveform models. In Section 4, we present the network architecture for passive SAR image reconstruction. In Section 5, we discuss parameterization and training of the network. We provide numerical simulations and discussion of the results in Section 6. Section 7 concludes the paper.

We use lower case bold fonts to denote vector quantities in finite dimensional spaces and upper case bold fonts to denote matrices.

2 Deep Learning Background

The most fundamental architecture in DL is the Artificial Neural Network, characterized by a cascade of affine mappings followed by point-wise nonlinear operations, referred to as *layers*. Each layer produces a *representation* $\mathbf{h} \in \mathbb{C}^M$ of its input $\mathbf{d} \in \mathbb{C}^N$, defined as

$$\mathbf{h} = \sigma(\mathbf{A}\mathbf{d} + \mathbf{b}) \quad (1)$$

where $\mathbf{A} \in \mathbb{C}^{M \times N}$ is the weight matrix, $\mathbf{b} \in \mathbb{C}^M$ is vector of corresponding biases, and $\sigma(\cdot)$ is an element-wise non-linear function, referred to as the activation function of the network. Letting Ω denote the input space, such that $\mathbf{d} \in \Omega$, the layer transforms Ω by (1) to create a feature space containing the representation \mathbf{h} .

At each layer, a new representation of the previous layer output is generated, resulting in a hierarchical representation of the input. The output at the end of the k^{th} layer can be written as

$$\mathbf{h}_k = \sigma(\mathbf{A}_k \mathbf{h}_{k-1} + \mathbf{b}_k). \quad (2)$$

Letting $\phi : \Omega_L \rightarrow \Gamma$ be a mapping from the feature space produced by the L^{th} layer, Ω_L , to the output space Γ , and redefining $\mathbf{d} = [\mathbf{d}, 1]^T$ and $\mathbf{W}_k = [\mathbf{A}_k, \mathbf{b}_k]$, $k = 0, \dots, L$, the network output $\mathbf{g}^* \in \Gamma$ becomes

$$\mathbf{g}^* = \phi(\mathbf{W}_L \sigma(\mathbf{W}_{L-1} \dots \sigma(\mathbf{W}_1 \sigma(\mathbf{W}_0 \mathbf{d}))). \quad (3)$$

(3) analytically defines the *network operator*, $\mathcal{L}(\theta) : \Omega \rightarrow \Gamma$, which is the mapping between the input and output spaces, where

$$\mathcal{L}(\theta)[\mathbf{d}] = \mathbf{g}^*, \quad \theta = \{\mathbf{W}_k\}_{k=1}^L. \quad (4)$$

In summary, the weights of the network provide a parametrization of the operation that the network performs, whereas the non-linear unit introduces the capacity to approximate complex mappings between input and output spaces. The nested non-linear transformations are generally explained in terms of the universal approximation theorem or probabilistic inference [51–53]. The mapping performed by the network operator is referred to as *forward propagation*.

Learning procedure in the network is the estimation of θ with respect to a figure of merit given a set of training data $\{\mathbf{d}_1, \mathbf{d}_2, \dots, \mathbf{d}_T\}$ and corresponding ground truth data set $G = \{\mathbf{g}_1, \mathbf{g}_2, \dots, \mathbf{g}_T\}$. This is achieved by optimizing a cost function with respect to network parameters θ , which typically defined as

$$\mathcal{J}_G[\theta] = \frac{1}{2T} \sum_{n=1}^T \|\mathcal{L}(\theta)[\mathbf{d}_n] - \mathbf{g}_n\|_2^2. \quad (5)$$

The analytic method of computing the derivatives through the network with respect to trainable parameters, θ , is referred to as the *backpropagation* algorithm. Network parameters θ are then updated via gradient descent such that

$$\theta^{l+1} = \theta^l - \eta_l \nabla_{\theta} \mathcal{J}_G[\theta^l] \quad (6)$$

where η_l is the step size of the l^{th} parameter update.

For large training sets, the gradient term $\nabla_{\theta} \mathcal{J}_G[\theta^l]$ is estimated as an average of the gradient values computed over a small subset of the training data. This methodology, referred to as Stochastic Gradient Descent (SGD), performs several gradient updates each time the full data is used. This update cycle is referred to as an "epoch."

The optimization over $\mathcal{J}_G[\theta]$ is typically a high-dimensional and non-convex problem. The error surface often consists of many saddle points and local minima [1, 54, 55]. As a result, a critical aspect of backpropagation is the initialization of the network parameters θ , which is typically chosen to guide the network to a locally optimal solution at backpropagation.

We propose DL framework for problems in which we have unknowns or uncertainties in the measurement model. In general, we can model a measurement mapping as

$$\mathbf{d} = \mathbf{F}(\theta)\boldsymbol{\rho} \quad (7)$$

where $\mathbf{d} \in \mathbb{C}^M$ are the measurements, $\boldsymbol{\rho} \in \mathbb{C}^N$ is the unknown quantity to be recovered, and $\mathbf{F}(\theta)$ is the measurement map that depends on the parameters θ . Following the DL framework for image reconstruction we introduced in [46], recovering the unknown $\boldsymbol{\rho}$ can be interpreted as learning a representation of the measurements \mathbf{d} in the image space. In this sense, DL framework captures the image reconstruction task at the forward propagation step. However, since θ is unknown and arbitrarily initialized, the reconstructed image is initially inaccurate.

The advantages of DL framework come at the backpropagation step, which allows the unknown parameters θ to be learned and to produce an accurate measurement map, thereby improving the accuracy of image reconstruction.

3 Passive Synthetic Aperture Radar Imaging

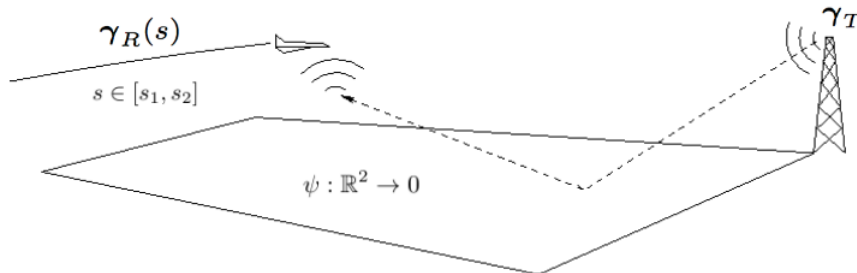


Figure 1: A depiction of the passive SAR configuration with flat topography $\psi(\mathbf{x})$. A stationary transmitter of opportunity located at γ_T , $\gamma_R : [s_1, s_2] \rightarrow \mathbb{R}^3$ denotes the receiver trajectory.

3.1 Imaging Geometry

Let $\mathbf{x} = [\mathbf{x}, \psi(\mathbf{x})] \in \mathbb{R}^3$ denote the position of a scatterer, where $\mathbf{x} = [x_1, x_2] \in \mathbb{R}^2$ and $\psi : \mathbb{R}^2 \rightarrow \mathbb{R}$ is a smooth function describing the ground topography.

We assume a stationary transmitter located at position $\boldsymbol{\gamma}_T \in \mathbb{R}^3$ and a moving receiver traversing a trajectory $\boldsymbol{\gamma}_R(s)$, where $s \in [s_1, s_2]$ denotes the slow-time variable. Figure 1 illustrates the passive SAR configuration under consideration. We assume that both the transmitter and receiver locations are known, but the transmitted waveforms are unknown.

3.2 Illuminators Of Opportunity

In this paper, we consider communication and broadcasting signals as the illuminators of opportunity. These signals are designed based on spread spectrum methodology and characterized by orthogonal division of the time or frequency domain to transmit different communication symbols. One such class of signals are orthogonal frequency division multiplexed (OFDM) waveforms. OFDM signals involve different phase or amplitude modulated symbols that are transmitted using a set of orthogonal waveforms spanning the channel bandwidth [56, 57].

OFDM signals have been widely studied as illuminators of opportunity due to the prevalence of DVB-T and WiMAX standards used throughout the world. [9, 11, 13, 14, 58–62]. Notably, the spectrum of an OFDM signal is relatively flat and noise-like over the channel [13, 61]. This characteristic can be observed by expressing the OFDM signal as a sum of random phase modulation symbols by applying the central limit theorem.

We assume that the transmitted waveforms may vary during receiver’s aperture time and model them as slow-time dependent as follows:

$$W(\omega, s) = \sum_{k=1}^K c_k \varphi_k(\omega, s) \quad (8)$$

where φ_k , $k = 1, \dots, K$, are basis functions and c_k , $k = 1, \dots, K$, are (possibly complex) corresponding coefficients. (8) provides a representation by which most common waveforms of opportunity can be modeled.

One such structure is that of binary or quadrature phase shift keying (B/QPSK) modulated signals which are building blocks of OFDM signals. Specifically, for QPSK, the basis coefficients are sampled uniformly on the unit circle, and the corresponding waveform has a flat spectrum. In our framework, we use this flat-spectrum structure as a statistical prior by the means of a constraint set in waveform estimation. The same process can be used to model more complex waveforms to find constraint sets for estimation.

3.3 Passive SAR Forward Model

Under the Born approximation and a flat topography assumption, we model the received signal as [63]

$$d(\omega, s) \approx W(\omega, s) \int e^{-i\frac{\omega}{c_0} R(s, \mathbf{x})} a(\mathbf{x}, s) \rho(\mathbf{x}) d\mathbf{x} \quad (9)$$

where

$$R(s, \mathbf{x}) = |\boldsymbol{\gamma}_T - \mathbf{x}| + |\boldsymbol{\gamma}_R(s) - \mathbf{x}| \quad (10)$$

is the bistatic range, $\omega \in [w_1, w_2]$ is the fast-time frequency, c_0 is the speed of light in free-space, $W(\omega, s)$ is the waveform transmitted at $s \in [s_1, s_2]$, and $a(\mathbf{x}, s)$ is the azimuth beam pattern. We let

$$\tilde{\mathcal{F}}(\omega, s)[\rho] := \int e^{-i\frac{\omega}{c_0} R(s, \mathbf{x})} a(\mathbf{x}, s) \rho(\mathbf{x}) d\mathbf{x} \quad (11)$$

and write (9) as

$$d(\omega, s) \approx W(\omega, s) \tilde{\mathcal{F}}(\omega, s)[\rho]. \quad (12)$$

Without loss of generality, we assume $a(\mathbf{x}, s)$ is constant and set it to 1. We note that, placing the origin at the center of the scene and invoking the far-field and small scene approximations for a sufficiently long

aperture, $\tilde{\mathcal{F}}$ can be further approximated to yield the following measurement model:

$$d(\omega, s) \approx W(\omega, s) e^{-i\frac{\omega}{c_0}(|\gamma_R(s)| + |\gamma_T|)} \int e^{i\frac{\omega}{c_0} \mathbf{k} \cdot \mathbf{x}} \rho(\mathbf{x}) d\mathbf{x} \quad (13)$$

where $\mathbf{k} = (\widehat{\gamma_R(s)} + \widehat{\gamma_T})^1$, and $\tilde{\mathcal{F}}$ is now approximated by the Fourier transform upto a phase factor.

We discretize the scene into an N -pixel grid of $X = \{\mathbf{x}_i\}_{i=1}^N$, and stack $\rho(\mathbf{x}_i)$, $i = 1, \dots, N$ into a vector $\boldsymbol{\rho} \in \mathbb{C}^N$. We discretize the fast-time frequency ω and slow-time s variables into $\{(\omega, s)_m\}_{m=1}^M$ pairs, and stack SAR measurements into a vector $\mathbf{d} \in \mathbb{C}^M$. With the same sampling scheme, we stack the sampled waveform elements $W(\omega, s)|_{(\omega, s)_m}$ into a vector $\mathbf{w} \in \mathbb{C}^M$. Thus, we obtain

$$\mathbf{d} \approx \text{diag}(\mathbf{w}) \tilde{\mathbf{F}} \boldsymbol{\rho} \quad (14)$$

where $\tilde{\mathbf{F}}$ is the matrix corresponding to the finite dimensional representation of $\tilde{\mathcal{F}}$ in (11).

3.4 Image Formation

Without complete knowledge of the forward model matrix $\mathbf{F} = \text{diag}(\mathbf{w}) \tilde{\mathbf{F}}$, we are no longer able to form bistatic SAR images using a two-layer filtered-backprojection type operation such as the one described in [63]. Similarly, optimization-based reconstruction approach is not applicable due to unknowns in the forward model. Since the dependence of the waveform coefficients to the forward model is multiplicative in the frequency domain, the problem of image reconstruction can be viewed as a blind deconvolution problem. A popular approach to solve such problems is to use an alternating minimization scheme which requires solution of two minimization problems at each iteration. In this work, we instead propose a data driven approach based on DL. The main advantage of the DL-based method is that it is task-driven. Instead of casting the unknown waveform as a joint parameter of the objective function in optimization, we cast it as a parameter of the optimizer. This results in conducting waveform estimation to specifically produce accurate imagery.

If the waveforms were known, estimation of the scene reflectivity could be formulated within Bayesian framework as the following optimization problem:

$$\boldsymbol{\rho}^* = \underset{\boldsymbol{\rho}}{\text{argmin}} \frac{1}{2} \|\mathbf{d} - \text{diag}(\mathbf{w}) \tilde{\mathbf{F}} \boldsymbol{\rho}\|_2^2 + \lambda \Phi(\boldsymbol{\rho}) \quad (15)$$

where the ℓ_2 -norm term represents the log-likelihood function under additive white Gaussian noise assumption, $\Phi(\boldsymbol{\rho})$ is the regularizer capturing the prior information on $\boldsymbol{\rho}$ and $\lambda > 0$ is the regularization parameter.

By deploying a convex Φ , the optimization can be implemented as a forward-backward splitting algorithm [64]. The forward-backward splitting algorithm takes the form of a gradient descent step over the smooth ℓ_2 -norm term, followed by a projection onto the feasible set defined by $\lambda \Phi$ as follows:

$$\boldsymbol{\rho}^{k+1} = \mathcal{P}_{\alpha\lambda\Phi}(\boldsymbol{\rho}^k - \alpha \nabla f[\boldsymbol{\rho}^k]) \quad (16)$$

where

$$f(\boldsymbol{\rho}) := \frac{1}{2} \|\mathbf{d} - \text{diag}(\mathbf{w}) \tilde{\mathbf{F}} \boldsymbol{\rho}\|_2^2, \quad (17)$$

$\alpha > 0$ is the step size and $\mathcal{P}_{\alpha\lambda\Phi}(\cdot)$ is the *proximity operator* of $\alpha\lambda\Phi(\boldsymbol{\rho})$ defined as

$$\mathcal{P}_{\alpha\lambda\Phi}(\boldsymbol{\rho}) = \underset{\mathbf{y}}{\text{argmin}} \frac{1}{2} \|\mathbf{y} - \boldsymbol{\rho}\|_2^2 + \alpha\lambda\Phi(\mathbf{y}). \quad (18)$$

When Φ is the indicator function of a closed convex set, the proximity operator is simply an orthogonal projection onto that set.

Using (17) and inserting $\nabla f[\boldsymbol{\rho}^k]$ into (16), we have

$$\boldsymbol{\rho}^{k+1} = \mathcal{P}_{\alpha\lambda\Phi}((\mathbf{I} - \alpha \tilde{\mathbf{F}}^H \text{diag}(|\mathbf{w}|^2) \tilde{\mathbf{F}}) \boldsymbol{\rho}^k + \alpha \tilde{\mathbf{F}}^H \text{diag}(\mathbf{w})^H \mathbf{d}) \quad (19)$$

where $|\mathbf{w}|^2$ denotes element-wise magnitude square of \mathbf{w} . Clearly, iterative reconstruction in (19) cannot be used without the knowledge of \mathbf{w} . Nevertheless, (19) serves as the foundation for the development of our DL-based approach discussed in Sections 4 and 5.

¹ $\hat{\mathbf{x}}$ denotes the unit vector in the direction of \mathbf{x}

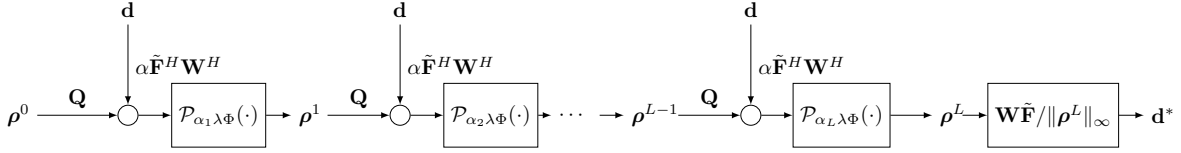


Figure 2: Proposed recurrent auto-encoder architecture with $\mathbf{W} = \text{diag}(\mathbf{w})$. The initial estimate $\boldsymbol{\rho}^0$ can be set according to preference (set as vector of zeros in this work). Following the estimate generated at layer L , a linear decoder maps the estimate back to the data space. Figure depicts the case in which different learning rates (α_i 's) are used at each iteration of the forward solver.

4 Network Architecture

Our goal is to implement a deep network that can recover scene reflectivity accurately when the waveform coefficients are unknown. To achieve this, we deploy the methodology of [46] for SAR imaging to simultaneously estimate the waveform and reconstruct the image. Specifically, we use a recurrent auto-encoder architecture [65]. A recurrent auto-encoder consists of a two stage network: a recurrent neural network (RNN) that emulates the iterative imaging algorithm defined by (19), and a *decoder* stage that maps the image estimate back to the measurement space. The main advantage of this architecture is that it allows for unsupervised training using the SAR received signal.

4.1 RNN-Encoder

RNNs fundamentally differ from other architectures since the parameters are shared over layers. As a result, in an RNN, each layer performs the same transformation between feature spaces. The RNN encoder is designed by unfolding the update equation in (19) for a fixed number of iterations, say L . This emulates the imaging algorithm described in Section 3. The corresponding weight matrix and bias are defined as

$$\mathbf{Q} = \mathbf{I} - \alpha \tilde{\mathbf{F}}^H \text{diag}(|\mathbf{w}|^2) \tilde{\mathbf{F}} \quad (20)$$

and

$$\mathbf{b} = \alpha \tilde{\mathbf{F}}^H \text{diag}(\mathbf{w})^H \mathbf{d}, \quad (21)$$

respectively. With this approach, the iterations become the feature transformations performed by the layers in (1) and we get the following update equation:

$$\boldsymbol{\rho}^{k+1} = \mathcal{P}_{\alpha \lambda \Phi}(\mathbf{Q} \boldsymbol{\rho}^k + \alpha \mathbf{F}^H \mathbf{d}) \quad (22)$$

where $\text{diag}(\mathbf{w}) \tilde{\mathbf{F}} = \mathbf{F}$. Thus, the image estimates $\boldsymbol{\rho}^k$, $k = 1, \dots, L$, become representations produced at the k^{th} layer of the network and the proximity operator $\mathcal{P}_{\alpha \lambda \Phi}(\cdot)$ becomes the network activation function².

While we motivate the network architecture from an optimization perspective, we modify the forward propagation in a way that deviates from this analogy. Notably, optimization by (22) is conducted over the complex domain to estimate the scene reflectivity. Furthermore, the proximal gradient method that our optimizer is based on requires a large number of iterations to converge. However, such a large number of layers is not practical from the point of view of training. Hence, we set L much smaller than the number of iterations needed for convergence. Additionally, we require the output of each layer to form visual representations of the received SAR signal. This is achieved by removing the phase of the representations in the network at forward propagation.

In the scope of this paper, we consider the recovery of sparse scenes and use ℓ_1 -norm constraint for Φ as the sparsity inducing prior.³ We note that the use of ℓ_1 -norm constraint is not a limitation of our

²Note that the regularizer must have closed form proximity operator that acts element-wise on its argument to construct a neural network.

³If the underlying scene is not sparse, a sparsifying transform such as the wavelet transform can be deployed. The optimization can then be re-formulated as recovery of sparse coefficients, in which weight and bias terms in (20) are represented by the composition of the forward map and the sparsifying transformation matrix.

framework as formulation with any Φ that has a well-defined, element-wise proximity operator leads to the same iterative form in (22). Therefore, we define the network non-linearity as a phaseless soft thresholding operator as follows:

$$\mathcal{P}_{\tau\ell_1}(\boldsymbol{\rho}) = \max(|\boldsymbol{\rho}| - \tau, 0), \quad \boldsymbol{\rho} \in \mathbb{C}^N \quad (23)$$

where $|\boldsymbol{\rho}|$ denotes taking the absolute value of the entries of $\boldsymbol{\rho}$, τ is the threshold determined by scaling of the ℓ_1 -norm constraint. With this modification, every representation in the RNN becomes a visual image, and feature mappings in (22) can be interpreted from an image processing perspective as discussed in Section 5.

4.2 Decoder

In implementing the decoder, we consider that scene reflectivities may be upper bounded given the operating frequencies of the receiver and typical scene refractive indices. Without loss of generality, we assume that the scene reflectivities vary between 0 and 1, and that the scene consists of at least one strong reflector. Under these assumptions, we normalize the final RNN output $\boldsymbol{\rho}^L$ before projection onto the measurement space as follows:

$$\boldsymbol{\rho}^* = \frac{\boldsymbol{\rho}^L}{\|\boldsymbol{\rho}^L\|_\infty}. \quad (24)$$

The normalization of the final output enhances the effect of learning in light of the expected range of reflectivity values in the reconstructed image.

Following the normalized image formation step, the decoder maps the estimate $\boldsymbol{\rho}^*$ back to the received signal space and synthesizes an estimate of the SAR measurement as follows:

$$\mathbf{d}^* = \text{diag}(\mathbf{w})\tilde{\mathbf{F}}\boldsymbol{\rho}^*. \quad (25)$$

By the insertion of the linear decoding layer (25), the network operator $\mathcal{L}[\theta]$ acts as an approximation to the identity map on the received signal space. Representing $\boldsymbol{\rho}^*$ as a function of network parameters θ and the input \mathbf{d} , we write

$$\mathcal{L}[\theta](\mathbf{d}) = \mathbf{d}^* := \text{diag}(\mathbf{w})\tilde{\mathbf{F}}\boldsymbol{\rho}^*(\theta, \mathbf{d}). \quad (26)$$

It is important to note that the final mapping back to received signal space allows the model to be trained in an *unsupervised* manner. This formulation offers a significant advantage. A supervised training scheme would require ground truth images coupled with SAR measurements. However, in the context of image reconstruction, a large number of SAR images acquired using the same imaging geometry may not be available. Moreover, training the RNN using SAR images would upper bound the performance by the reconstruction quality of conventional imaging algorithms that formed the SAR images in the first place. Our approach avoids these drawbacks by unsupervised training.

5 Network Training

5.1 Forward Propagation For SAR Imaging

Consider the ideal expressions for the network weight matrix and bias terms in (20) with the true underlying waveform. Then, the normal operator $\mathbf{F}^H\mathbf{F}$ is a spatially varying filter of low pass characteristic. Essentially the map \mathbf{Q} is merely composed of an all pass filter \mathbf{I} of scale one, and a low pass filter of scale $-\alpha M$. Since $\alpha M \ll 1$, \mathbf{Q} acts as an image domain filter that gradually suppresses all frequencies by $1 - \alpha M$ factor, except the high frequency bands determined by the cutoffs of the rows of $\mathbf{F}^H\mathbf{F}$.

The result of the linear filtering operation is then *biased* towards the backprojection estimate by addition of the term $\mathbf{b} = \alpha\mathbf{F}^H\mathbf{d}$. Since $\tilde{\mathbf{F}}$ is sampled from a Fourier Integral Operator [63], we know that backprojection preserves the target placement and edges in the image. Hence the biasing step practically enhances the foreground of the output of the filtering operation. As the mid to low frequency components are gradually suppressed due to repetitive application of \mathbf{Q} through the network, the edges get further enhanced by the biasing due to their high frequency content. Thereby, pixel-wise absolute thresholding at each layer effectively performs background suppression rather than suppressing the foreground, and the composite map of the layer essentially becomes a non-linear enhancement filter.

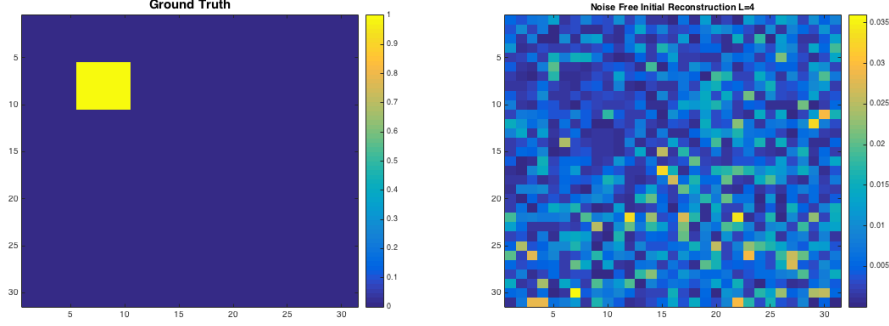


Figure 3: Ground truth image used in experiments (left) vs. the image reconstructed by the RNN encoder with the randomly initialized waveform coefficients (right). The target is completely lost and suppressed in background noise due to the mismatch introduced by the wrong waveform in reconstruction.

However, as emphasized throughout the paper, forward map \mathbf{F} is not fully known and at initialization the network cannot perform these operations accurately due to an arbitrary initial \mathbf{w} . Let $\mathbf{w} = \mathbf{w}^0$ be a randomly picked waveform coefficient vector to initialize the network parameters \mathbf{Q} and \mathbf{b} . Setting the initial image estimate fed to the network as $\boldsymbol{\rho}^0 = 0$, the representation at the first layer becomes

$$\boldsymbol{\rho}^1 = \max(|\alpha \tilde{\mathbf{F}}^H \text{diag}(\mathbf{w}^0)^H \mathbf{d}| - \alpha \lambda, 0). \quad (27)$$

We define $\tilde{\boldsymbol{\rho}}$ as the intermediate estimate resulting from the backprojection with its j^{th} pixel value given as

$$\tilde{\rho}_j := [\tilde{\mathbf{F}}^H \text{diag}(\mathbf{w}^0)^H \mathbf{d}]_j = \sum_{k=1}^M (\overline{\mathbf{w}^0})_k \overline{(\tilde{\mathbf{F}})}_{kj} \mathbf{d}_k, \quad j = 1, 2, \dots, N. \quad (28)$$

Plugging in (14) into (28), and breaking down the contributions of pixels with indices $i = j$ and $i \neq j$ into the estimate of the reflectivity at j^{th} pixel, we obtain

$$\tilde{\rho}_j = \rho_j \left(\sum_{k=1}^M (\overline{\mathbf{w}^0})_k (\mathbf{w}_t)_k \right) + \sum_{k=1}^M \sum_{i \neq j} \overline{(\tilde{\mathbf{F}})}_{kj} (\tilde{\mathbf{F}})_{ki} (\overline{\mathbf{w}^0})_k (\mathbf{w}_t)_k \rho_i \quad (29)$$

where \mathbf{w}_t is the vector of true waveform coefficients, and ρ_j , $j = 1, \dots, N$ are the elements of the true scene $\boldsymbol{\rho}$.

Consider a passive imaging scenario such that the true waveform coefficients are sampled from a QPSK signal, and that we set entries of \mathbf{w}^0 with randomly picked symbols from the unit circle in \mathbb{C} . Since such a randomly initialized \mathbf{w}^0 is highly unlikely to be correlated to the true QPSK waveform, the contribution of the underlying scene pixel ρ_j to its estimate $\tilde{\rho}_j$ diminishes. Furthermore, this contribution is diminished to a level comparable to that of other points in the underlying scene ρ_i where $i \neq j$. As all scene reflectivities are scaled by low correlated complex exponentials in (29), targets get suppressed and a noisy image is obtained by backprojection. This phenomenon is observed in Figure 3 from the reconstruction performance with a randomly initialized waveform. Therefore, obtaining a highly correlated waveform coefficient vector \mathbf{w} is essential for the reconstruction process by (22).

5.2 Backpropagation For Waveform Estimation

Instead of parameterizing the feature maps of the RNN by the weight matrix \mathbf{Q} and the bias vector \mathbf{b} , we limit parameterization only to the waveform vector \mathbf{w} . Thereby, backpropagation is cast as a solver for the waveform estimation problem. Furthermore, splitting the waveform as a parameter preserves the known components of \mathbf{Q} and \mathbf{b} , which are initialized using $\tilde{\mathbf{F}}$.

In addition to the unknown waveform in the passive SAR forward model, the optimization hyperparameters can be also learned. For our model, we include threshold parameter of the network non-linearity,

initialized as $\tau = \alpha\lambda$ into learning, and define network parameter as $\theta = \{\mathbf{w}, \tau\}$.

Given training data $D = \{\mathbf{d}_1, \mathbf{d}_2 \cdots \mathbf{d}_T\}$, we search a minimizer over the parameter space $\{\mathbf{w}, \tau\}$ for the following cost function:

$$\mathcal{J}_D(\mathbf{w}, \tau) = \frac{1}{T} \sum_{n=1}^T \ell(\text{diag}(\mathbf{w})\tilde{\mathbf{F}}\boldsymbol{\rho}_n^*, \mathbf{d}_n) \quad (30)$$

where ℓ is a properly chosen loss function. For ℓ , we pick the ℓ_2 -norm of the mismatch between the data synthesized by the network and the input data. Furthermore, we incorporate constraints into the cost function to enforce prior information on \mathbf{w}, τ . Most significantly, we focus our attention to constraint the underlying waveform by a priori functional form. For our problem, we consider that the unknown waveform coefficients are sampled from a flat spectrum signal, and restrict \mathbf{w} to have unit modulo entries. For τ , we invoke a non-negativity constraint, and formulate backpropagation problem as

$$BP := \underset{\mathbf{w}, \tau}{\text{minimize}} \frac{1}{T} \sum_{n=1}^T \|\text{diag}(\mathbf{w})\tilde{\mathbf{F}}\boldsymbol{\rho}_n^* - \mathbf{d}_n\|_2^2 + i_{C_{\mathbf{w}}}(\mathbf{w}) + i_{C_{\tau}}(\tau) \quad (31)$$

where $i_C(\cdot)$ denotes the indicator function of subscript set C , $C_{\mathbf{w}}$ and C_{τ} denote constraint sets on parameters \mathbf{w} and τ , respectively. The minimization is then performed by projected SGD. Taking gradient steps over the smooth \mathcal{J}_D term, and projecting onto constraint sets $C_{\mathbf{w}}$ and C_{τ} , we obtain the updates as

$$\mathbf{w}^{l+1} = \mathcal{P}_{C_{\mathbf{w}}} \left(\mathbf{w}^l - \eta \frac{1}{|B|} \sum_{n \in I_B} \nabla_{\mathbf{w}} \ell(\text{diag}(\mathbf{w})\tilde{\mathbf{F}}\boldsymbol{\rho}_n^*, \mathbf{d}_n) \Big|_{\theta=\theta^l} \right), \quad (32)$$

$$\tau^{l+1} = \mathcal{P}_{C_{\tau}} \left(\tau^l - \eta \frac{1}{|B|} \sum_{n \in I_B} \frac{\partial \ell(\text{diag}(\mathbf{w})\tilde{\mathbf{F}}\boldsymbol{\rho}_n^*, \mathbf{d}_n)}{\partial \tau} \Big|_{\theta=\theta^l} \right) \quad (33)$$

where $\theta^l = \{\mathbf{w}^l, \tau^l\}$ denotes the parameter values at the l^{th} iteration in backpropagation, η is the learning rate (or step-size), $B \subseteq D$ is the randomly selected subset of the training data, $|B|$ is the cardinality of the subset B , I_B is an index set corresponding to B . \mathcal{P}_C denotes the projection operator corresponding to the constraint set C such that for the specified constraints for \mathbf{w} and τ , we have

$$(\mathcal{P}_{C_{\mathbf{w}}}(\tilde{\mathbf{w}}))_i = \frac{\tilde{\mathbf{w}}_i}{|\tilde{\mathbf{w}}_i|}, \quad \mathcal{P}_{C_{\tau}}(\tilde{\tau}) = \max(\tilde{\tau}, 0). \quad (34)$$

As mentioned earlier, due to the nested non-linear structure of the recurrent auto-encoder estimator, (30) is a highly non-convex optimization problem. In addition, first order methods are prone to converging to local minima which adds further difficulty to estimation of \mathbf{w} . However, our parameterization enforces the problem structure of SAR imaging, and places the network in a neighborhood over the loss surface only upto a diagonal multiplier of the true forward model, along with any prior knowledge of the functional form of \mathbf{w} . Therefore, by the updates in (6), a stationary point in the neighborhood of a strong initial point is searched. Hence, backpropagation is used as a tool for *refining* the SAR forward model and improving image reconstruction implemented by forward propagation.

5.3 Network Derivatives

An important consideration is the computation of the backpropagation equation for waveform coefficients. Since the objective being minimized is a real valued function of a complex variable \mathbf{w} , we have to perform complex backpropagation on the parameters defined as

$$\nabla_{\mathbf{w}} \ell = \overline{\left(\frac{\partial \ell}{\partial \mathbf{w}} \right)} \quad (35)$$

where $\overline{(\cdot)}$ denotes complex conjugation and the partial derivative in (35) is the Wirtinger derivative [66].

Notably, \mathbf{w} parameterizes both \mathbf{Q} and $\mathbf{F} = \text{diag}(\mathbf{w})\tilde{\mathbf{F}}$. Writing the partial derivative of the loss function ℓ with respect to \mathbf{w} , from the chain rule we have

$$\frac{\partial \ell(\mathbf{d}^*, \mathbf{d})}{\partial \mathbf{w}} = \frac{\partial \mathbf{Q}}{\partial \mathbf{w}} \frac{\partial \ell(\mathbf{d}^*, \mathbf{d})}{\partial \mathbf{Q}} + \frac{\partial \mathbf{F}}{\partial \mathbf{w}} \frac{\partial \ell(\mathbf{d}^*, \mathbf{d})}{\partial \mathbf{F}}. \quad (36)$$

Hence, we compute the derivative with respect to \mathbf{w} by first computing derivatives with respect to $\{\mathbf{Q}, \mathbf{F}\}$ as

$$\begin{aligned} \frac{\partial \ell(\mathbf{d}^*, \mathbf{d})}{\partial \mathbf{Q}} &= \frac{\partial \rho^*}{\partial \mathbf{Q}} \frac{\partial \ell(\mathbf{d}^*, \mathbf{d})}{\partial \rho^*}, \\ \frac{\partial \ell(\mathbf{d}^*, \mathbf{d})}{\partial \mathbf{F}} &= \frac{\partial \rho^*}{\partial \mathbf{F}} \frac{\partial \ell(\mathbf{d}^*, \mathbf{d})}{\partial \rho^*} + \left(\frac{\partial \mathbf{F}}{\partial \mathbf{F}} \rho^* \right) (\bar{\mathbf{d}}^* - \bar{\mathbf{d}}). \end{aligned} \quad (37)$$

The derivative with respect to τ is simply the real valued ⁴ partial derivative of the form

$$\frac{\partial \ell(\mathbf{d}^*, \mathbf{d})}{\partial \tau} = \frac{\partial \rho^*}{\partial \tau} \frac{\partial \ell(\mathbf{d}^*, \mathbf{d})}{\partial \rho^*}. \quad (38)$$

The second component of the derivative with respect to \mathbf{F} in (37) originates from having the linear decoder stage that projects the image estimate ρ^* to the received signal space by \mathbf{F} . We note that in that expression, the partial derivative of \mathbf{F} with respect to itself yields an identity tensor of size $M \times N \times M \times N$, which multiplies the image estimate $\rho^* \in \mathbb{R}^N$ to yield an $M \times N \times M$ tensor. We provide a detailed derivation of network derivatives in Appendix A.1.

To backpropagate through the recurrent encoder component, we use backpropagation through time algorithm (BPTT). Since the parameters $\{\mathbf{Q}, \mathbf{F}, \tau\}$ are shared among layers, and only the error resulting from only the final layer is considered in the optimization, BPTT computes the derivatives in the RNN-encoder as follows:

$$\frac{\partial \rho^*}{\partial \theta} = \left(\sum_{i=1}^L \frac{\partial \rho^k}{\partial \theta} \frac{\partial \rho^L}{\partial \rho^k} \right) \frac{\partial \rho^*}{\partial \rho^L} \quad (39)$$

where ρ^k , $k = 1, \dots, L$ is the network representation generated at the k^{th} layer.

Despite the general form we present in this section, a distinct effect of the flat spectrum constraint we place on \mathbf{w} for signals such as QPSK or OFDM can be observed at backpropagation. As explicitly shown in (20), \mathbf{Q} only has dependence on \mathbf{w} through its element-wise modulus by the $\text{diag}(|\mathbf{w}|^2)$ term. By setting initial \mathbf{w}^0 as a unit modulo entry signal, and projecting \mathbf{w} iterates onto the unit sphere in \mathbb{C}^M by (32), $\text{diag}(|\mathbf{w}|^2)$ is merely the identity matrix and \mathbf{Q} is effectively fixed through the training procedure. Therefore its dependence to the network parameterization is dropped. Removing the contribution of \mathbf{Q} to the partial derivative in (36) yields the following final update form for the parameter \mathbf{w} :

$$\frac{\partial \ell(\mathbf{d}^*, \mathbf{d})}{\partial \mathbf{w}} = \frac{\partial \mathbf{F}}{\partial \mathbf{w}} \left[\left(\sum_{i=1}^L \frac{\partial \rho^k}{\partial \mathbf{F}} \frac{\partial \rho^L}{\partial \rho^k} \right) \frac{\partial \rho^*}{\partial \rho^L} \frac{\partial \ell(\mathbf{d}^*, \mathbf{d})}{\partial \rho^*} + \left(\frac{\partial \mathbf{F}}{\partial \mathbf{F}} \rho^* \right) (\bar{\mathbf{d}}^* - \bar{\mathbf{d}}) \right]. \quad (40)$$

6 Numerical Simulations

6.1 Scene and Imaging Parameters

We assume isotropic transmit and receive antennas, and simulate a transmitted signal with bandwidth and center frequency of 8MHz and 760MHz, respectively. The simulated waveform is modulated using QPSK, in which the symbols are generated from an i.i.d. uniform distribution. This corresponds to approximately 20m range resolution for monostatic SAR. Thus, we simulate a 620×620 m² scene and discretize it into 31×31 pixels as shown in Figure 3.

⁴Both partial derivatives in the chain rule of (38) are both real valued, due to having a real valued loss function, image estimate and variable.

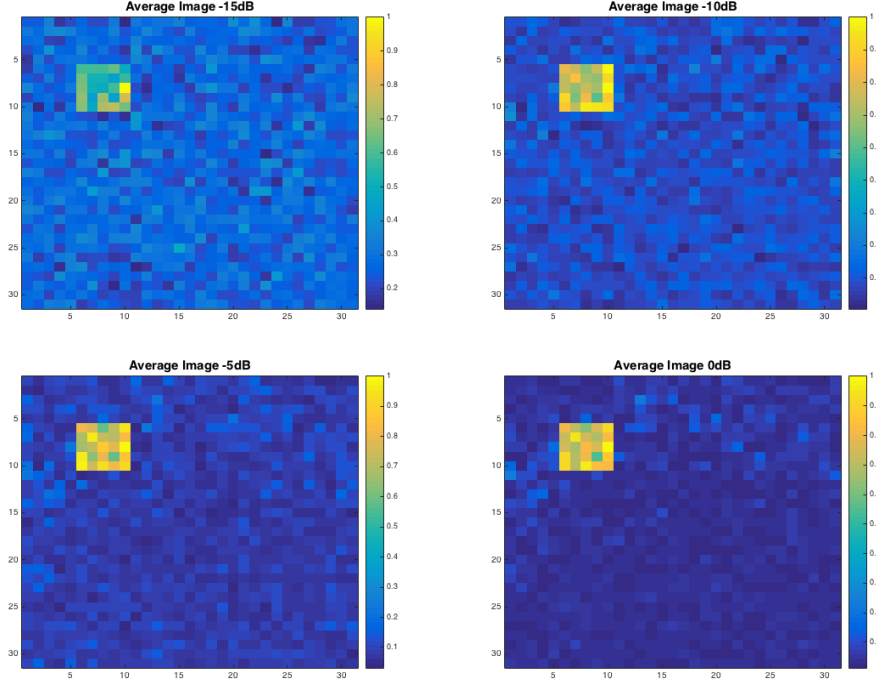


Figure 4: Reconstructed average images by the proposed model under -15 dB, -10 dB, -5 dB and 0 dB SNR levels at data collection for training and test sets. Each image is formed by averaging the 20 test samples under different realizations at the same SNR. The model has learned suitable parameters such that imaging performance is drastically improved over the initialization image for every noise level under consideration.

The receiver antenna traverses a circular trajectory, defined as $\gamma_R(s) = [7 \cos(s), 7 \sin(s), 6.5]$ km. The transmitter is fixed and located at $\gamma_T = [11.2, 11.2, 6.5]$ km. The aperture is sampled uniformly into 128 uniform samples, and the bandwidth is sampled uniformly into 64 samples.

6.2 Training Data

We generate six different training sets consisting of randomly generated sparse scenes with a single point or extended target that varies in rectangular shape and location. The length and width of each rectangular target are sampled from a uniform distribution in the range $[1, 6]$. The targets are placed randomly within the range of $[3, 28] \times [3, 28]$ pixels. We then generate SAR data for each image using the full forward model in (14) described in Section 3. In each training set, we add a realization of white Gaussian noise at specified SNR level to each sample. The model is trained using each training set separately to test the robustness under different noise levels. We consider SNR levels of -20 , -15 , -10 , -5 , 0 and 10 dB in SAR measurements collected from randomly generated scenes.

For data collection, we envision a two-stage protocol to form training and test sets as proposed in [46]. In the first stage, an airborne receiver collects test data from a scene of interest. In the second stage, several reflectors are placed in the scene to form either extended or point targets and training data is collected under the same imaging geometry as before. Note that neither the location nor the shape of the foreground scatterers need to be known in order to use the training data in our unsupervised training scheme.

6.3 Test Data

In testing we use measurements collected from a single scene of interest. The test scene is displayed in Figure 3 and backscattered field is generated by the forward model in (14). 20 different realizations of white Gaussian noise at -20 , -15 , -10 , -5 , 0 and 10 dB SNR are used to form 6 sets each consisting of 20 samples of SAR measurements. Each test set is fed into the model trained with the corresponding noise level of SAR

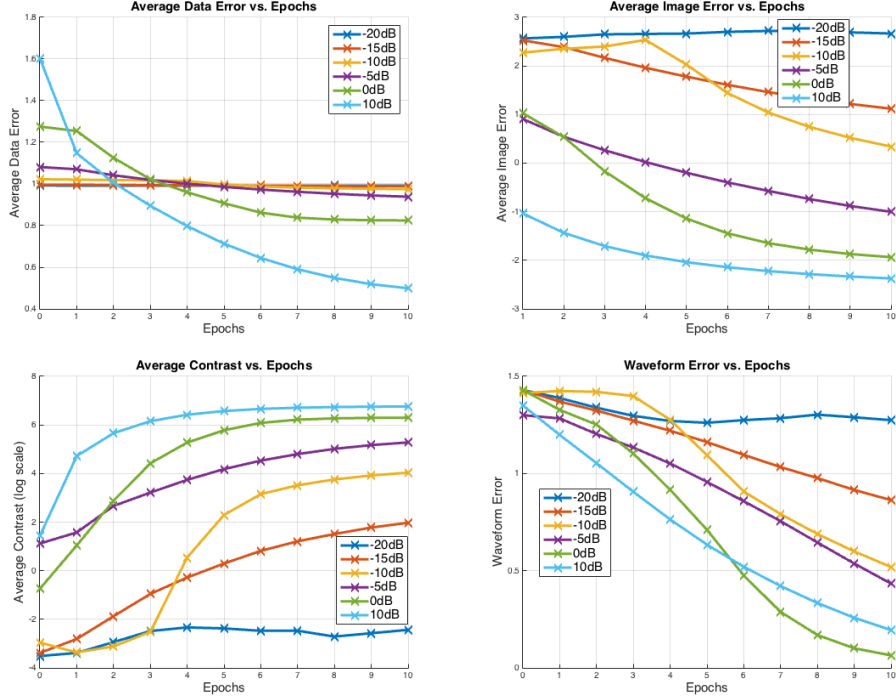


Figure 5: Average values of the proposed data mismatch (41), image mismatch and contrast (42) and waveform error (43) metrics over 20 test samples at -20 , -15 , -10 , -5 , 0 and 10 dB SNR cases. Curves are obtained from reconstruction results with the parameter estimates generated by the network at each epoch, trained with SAR measurements under corresponding SNR.

measurements. We evaluate the reconstruction performance as the average over 20 results for statistical accuracy.

6.4 Network Design and Initialization

We implement the proposed network with an RNN-encoder of $L = 4$ layers, and activation function as the phaseless soft-thresholding function introduced in Section 4. The model is trained for 10 epochs for each experiment. We limit the number of training samples based on the results of our previous study [46] and set it to 10. Hence we perform batch gradient descent, which corresponds to a single parameter update per epoch. We use an adaptive learning rate of $\eta_l = \eta_0 / (1 + l)$ in training, where $l = 1, \dots$ is the index of the epoch, with an initial step size of $\eta_0 = 1e - 4$. The learning rate η_l for the threshold parameter τ is scaled by a factor of $1e - 6$ for -15 and -20 dB cases, $1e - 7$ for the others.

The network weight matrix and bias terms are initialized with the known components of the forward model \mathbf{F} in (26). We set the initial regularization parameter as $\lambda = 10$, and set $\alpha = 1e - 5$, upper bounded by the reciprocal of the largest eigenvalue of $\tilde{\mathbf{F}}^H \tilde{\mathbf{F}}$. To keep the number of unknowns at a reasonable level, we assume that waveforms are static with respect to the slow-time variable. As demonstrated in Section 5, we constrain the parameter \mathbf{w} using the QPSK properties, and project the entries of \mathbf{w} at each update onto the unit ball in \mathbb{C}^M , as in (32). We initialize \mathbf{w} by the real valued flat spectrum signal of all ones instead of random initialization to standardize our evaluation of different experiments.

6.5 Performance Evaluation

We evaluate the reconstruction performance on the image and waveform coefficients using the following figures of merit.

$$L_d(\boldsymbol{\rho}^{*l}) = \frac{\|\text{diag}(\mathbf{w}^l) \tilde{\mathbf{F}}(\boldsymbol{\rho}^*)^l - \mathbf{d}\|_2^2}{\|\mathbf{d}\|_2^2} \quad (41)$$

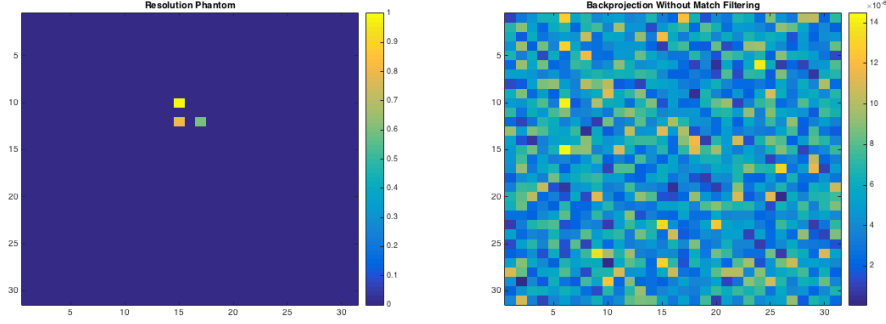


Figure 6: Phantom used to evaluate resolution and the linearly reconstructed image from directly backprojecting data at -10 dB SNR. The point targets are located in range bins 15 and 17, cross range bins 10 and 12.

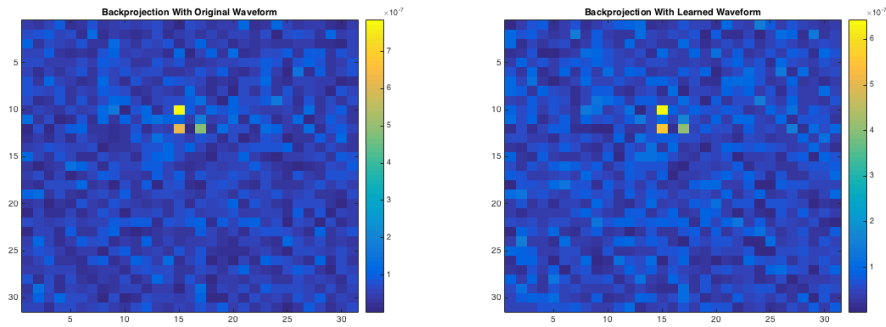


Figure 7: Linearly reconstructed phantom image by first match filtering with the ground truth waveform coefficients and coefficients learned with the proposed model respectively, followed by backprojection, at -10 dB SNR.

measures the normalized data domain mismatch of the reconstructed image.

$$L_{\rho}(\rho^*) = \frac{\|\rho^* - \rho\|_2^2}{\|\rho\|_2^2}, \quad C_{\rho}(\rho^*) = \frac{|\mathbb{E}[\rho_f^*] - \mathbb{E}[\rho_b^*]|^2}{\text{var}[\rho_b^*]} \quad (42)$$

measure the normalized image domain error with respect to the ground truth testing image, and the contrast in the reconstructed image, respectively.

$$L_{\mathbf{w}_t}(\mathbf{w}^l) = \frac{\|\mathbf{w}_t - \mathbf{w}^l\|^2}{\|\mathbf{w}_t\|^2} \quad (43)$$

measures the normalized waveform mismatch with respect to the ground truth QPSK coefficients. $(\rho^*)^l$ denotes the normalized image generated by the RNN encoder, with the parameters obtained at epoch l , ρ is the ground truth image. \mathbf{w}_t is the ground truth waveform coefficient vector and \mathbf{w}^l is the learned waveform coefficient vector at epoch l . ρ_f^* and ρ_b^* are the foreground and background components of the reconstructed image, respectively. $\mathbb{E}[\cdot]$ stands for statistical expectation, $\text{var}[\cdot]$ stands for statistical variance and \mathbf{d} is the input SAR data. Curves corresponding to each SNR value demonstrate the performance of the model trained on measurements corresponding to that noise level, and evaluated on test samples collected at the same SNR.

In order to evaluate the resolution improvement achieved by learning, we examine the bias terms of the DL-based model. This corresponds to evaluation of backprojection reconstruction following matched filtering with the learned waveform coefficients. We compare the peak and average background of the reconstructed image with learned waveform coefficients to the one obtained with the true waveform, and to that of reconstruction by backprojection without match-filtering. Essentially, the last case is equivalent to

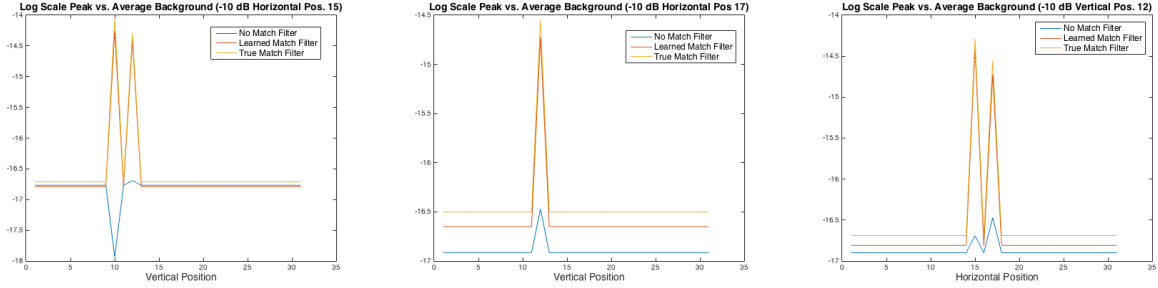


Figure 8: Cross sections of linearly reconstructed images at -10 dB SNR in Figures 6, and 7. The background pixels at the cross section are averaged to depict the noise level with respect to peak values. All values displayed in logarithmic scale.

the initial waveform set to all 1’s in its bandwidth. Evaluation is performed on the phantom displayed in Figure 6, with respect to how the two point targets are resolved in horizontal and vertical directions, as well as how the weak point target in (12,17) is resolved from the background noise in our evaluations.

6.6 Results

Our simulations show that the DL-based approach achieves highly accurate reconstruction performance under SNR scenarios above -20 dB for all metrics under consideration. To display the performance visually, we present the reconstructed images by the model under SNR levels of -15 , -10 , -5 , and 0 dB in Figure 4. The images displayed in the figure demonstrate the impact of waveform and threshold learning by the DL-based method as described in Section 5.1. Fixing the image domain filters by the constraints on \mathbf{w} , learning the waveform coefficients become equivalent to refining the backprojection image. Hence, waveform learning directly impacts the placement and strength of target pixels, whereas threshold learning controls the amount of background suppression in the image. The impact of threshold learning is most visible in the -15 dB image, as the higher threshold learning rate than the other experiments yields similar background suppression while trading off gradual suppression of targets pixels. It is observed in Figure 4 that clear background suppression and geometric fidelity of the extended target are achieved by our method despite initializing the model with a waveform that has poor correlation to the true one. Moreover, image contrast and image mismatch metrics, as well as the decay in waveform error shown in Figure 5 validate the main arguments of our approach, as the waveform coefficients are learned to the extent of high correlation with the underlying QPSK signal such that the model produces enhanced imagery.

As expected, the performance of the method degrades gracefully as the noise level increases both in image reconstruction and waveform estimation. For the -20 SNR case, the gradual improvement in the waveform is insufficient to impact reconstruction performance as indicated by negligible changes in image domain metrics as shown in Figure 5. However, the drastic impact of waveform estimation can be observed in the -10 dB case. Despite no indicative improvement on the data mismatch function over epochs similar to the -20 dB case, the algorithm learns a much more correlated waveform coefficient which improved the reconstruction performance significantly.

We demonstrate the resolution performance of the DL-based method for the -10 dB case as discussed in Section 6.5. The reconstructed images by backprojection after match-filtering with initial, true and learned waveform coefficients are provided in Figures 6 and 7, respectively. Reconstruction using the waveform coefficients learned by the DL-based approach produces a nearly identical image as the one produced using the true waveform, which is clearly superior in recovering and resolving point targets compared to the initial point. This can also be observed in the cross-sections at horizontal and vertical directions that contain target pixels, which are provided in Figure 8 in log-scale. The peak and average background values at each cross-section of the reconstructed image using learned waveform coefficients are highly consistent with the ones obtained with true waveform coefficients. Notably, such accuracy in image reconstruction is obtained despite a final normalized waveform mismatch of 0.5 as shown in Figure 5, which indicates robustness of the method to errors in estimation.

Overall, it can be concluded from our experiments that learning a correlated waveform is sufficient to obtain improved imagery. The model offers considerable robustness to measurement noise even with limited number of training samples, which increases the applicability of our method in real world scenarios. However, the limited performance in the -20 dB scenario can be traced to the limited number of samples used in training. The poor improvement of waveform error suggests the gradient estimates are highly contaminated by noise, which can be avoided by averaging over more samples. Handling such high noise scenarios may require accurate initialization, or more structural constraints on the functional form of the waveform, as well as increasing the number of training samples.

7 Conclusion

In this paper, we presented a novel deep learning based approach for simultaneous estimation of the scene reflectivity and transmitted waveform. Our method requires a single receiver, providing reduced cost and improved simplicity over existing methods such as PCL and TDOA/FDOA. We consider the passive scenario in which the transmitter location is known, but the transmitted waveform is unknown. We approach image reconstruction from Bayesian framework and set up an optimization problem to estimate the scene reflectivity. We formulate a proximal gradient descent algorithm to solve for the scene reflectivity, which we unfold for a fixed number of iterations to formulate a RNN parameterized by waveform coefficients. Hence, for a given waveform coefficient vector, the RNN becomes a solver for the scene reflectivity at forward propagation, and waveform coefficients become parameters that can be estimated by backpropagation.

We then cascade the RNN with a decoding layer consisting of normalization and a linear forward map that synthesizes SAR measurements from the reconstructed scene reflectivities resulting in a recurrent auto-encoder architecture. Thereby, we learn the transmitted waveform in an unsupervised manner by minimizing the mismatch between a set of received SAR signals and corresponding SAR measurements synthesized by the network. At backpropagation, we utilize a flat spectrum constraint on the waveform by performing updates via projected stochastic gradient descent. Hence, the framework we formulate has applicability to wide range of spread spectrum signals that are common to transmitters of opportunity. The main advantage of our method is that the waveform estimation is performed in a task driven manner. The DL-based model ultimately estimates waveform coefficients with the goal of producing accurate imagery with forward propagation. Moreover, the structural form for the transmitted signals is merely used as a prior by the means of a constraint set in our framework, and lack thereof does not limit our formulation.

We demonstrate the performance of our deep learning approach with numerical simulations, showing that with a limited number of SAR received signals collected at realistic SNR levels, the model estimates QPSK modulated signals in a manner that produces accurate SAR imagery. Furthermore, we show that our DL-based method is robust to estimation errors as it reconstructs highly consistent images to the ones obtained by the true underlying waveform even in the presence of a non-negligible mismatch in learned and true waveform coefficients. In future, we will further pursue improving the performance of our method in the low SNR scenarios, and test the estimation quality with other waveforms such as OFDM signals.

Acknowledgement

B. Yonel and B. Yazici were supported by the Air Force Office of Scientific Research (AFOSR) under the agreements under the agreement FA9550-16-1-0234. E. Mason is supported by the Naval Research Laboratory.

References

- [1] Y. LeCun, Y. Bengio, and G. Hinton, “Deep learning,” *Nature*, vol. 521, no. 7553, pp. 436–444, 2015.
- [2] H. Greenspan, B. van Ginneken, and R. M. Summers, “Guest editorial deep learning in medical imaging: Overview and future promise of an exciting new technique,” *IEEE Transactions on Medical Imaging*, vol. 35, no. 5, pp. 1153–1159, 2016.

- [3] G. Litjens, T. Kooi, B. E. Bejnordi, A. A. A. Setio, F. Ciompi, M. Ghafoorian, J. A. van der Laak, B. van Ginneken, and C. I. Sánchez, “A survey on deep learning in medical image analysis,” *Medical image analysis*, vol. 42, pp. 60–88, 2017.
- [4] K. He, X. Zhang, S. Ren, and J. Sun, “Deep residual learning for image recognition,” in *Proceedings of the IEEE conference on computer vision and pattern recognition*, 2016, pp. 770–778.
- [5] C. Dong, C. C. Loy, K. He, and X. Tang, “Image super-resolution using deep convolutional networks,” *IEEE transactions on pattern analysis and machine intelligence*, vol. 38, no. 2, pp. 295–307, 2016.
- [6] Y. Bengio *et al.*, “Learning deep architectures for ai,” *Foundations and trends® in Machine Learning*, vol. 2, no. 1, pp. 1–127, 2009.
- [7] Y. Bengio, A. Courville, and P. Vincent, “Representation learning: A review and new perspectives,” *IEEE Trans. Pattern Analysis and Machine Intelligence*, vol. 35, no. 8, pp. 1798–1828, Aug 2013.
- [8] C. Yarman, L. Wang, and B. Yazici, “Doppler synthetic aperture hitchhiker imaging,” *Inverse Problems*, vol. 26, no. 6, p. 065006, 2010.
- [9] M. Malanowski, K. Kulpa, M. Dryjanski, and S. Pietrzyk, “Fixed WiMAX (IEEE 802.16d) base station signal analysis for passive radar applications,” *Proc. SPIE*, vol. 7502, pp. 75 020V–75 020V–6, 2009. [Online]. Available: <http://dx.doi.org/10.1117/12.837900>
- [10] B. Dawidowicz, P. Samczynski, M. Malanowski, J. Misiurewicz, and K. Kulpa, “Detection of moving targets with multichannel airborne passive radar,” *Aerospace and Electronic Systems Magazine, IEEE*, vol. 27, no. 11, pp. 42–49, November 2012.
- [11] M. Rapson, “Passive multistatic radar imaging using an OFDM based signal of opportunity,” Ph.D. dissertation, Air Force Institute of Technology, 2012.
- [12] P. Stinco, M. S. Greco, F. Gini, and A. Farina, “Posterior crammer lower bounds for passive bistatic radar tracking with uncertain target measurements,” *Signal Processing*, vol. 93, no. 12, pp. 3528 – 3540, 2013, special Issue on Advances in Sensor Array Processing in Memory of Alex B. Gershman. [Online]. Available: <http://www.sciencedirect.com/science/article/pii/S0165168413000832>
- [13] J. Palmer, H. Harms, S. Searle, and L. Davis, “DVB-T passive radar signal processing,” *Signal Processing, IEEE Transactions on*, vol. 61, no. 8, pp. 2116–2126, April 2013.
- [14] J. Gutierrez del Arroyo and J. , “WiMAX OFDM for passive SAR ground imaging,” *Aerospace and Electronic Systems, IEEE Transactions on*, vol. 49, no. 2, pp. 945–959, APRIL 2013.
- [15] M. Malanowski, R. Haugen, M. Greco, D. O’Hagan, R. Plsek, and A. Bernard, “Land and sea clutter from FM-based passive bistatic radars,” *Radar, Sonar Navigation, IET*, vol. 8, no. 2, pp. 160–166, February 2014.
- [16] L. Wang, I.-Y. Son, and B. Yazici, “Passive imaging using distributed apertures in multiple-scattering environments,” *Inverse Problems*, vol. 26, no. 6, p. 065002, 2010.
- [17] L. Wang and B. Yazici, “Passive imaging of moving targets using sparse distributed apertures,” *SIAM Journal on Imaging Sciences*, vol. 5, no. 3, pp. 769–808, 2012.
- [18] E. Mason, I. Y. Son, and B. Yazici, “Passive synthetic aperture radar imaging using low-rank matrix recovery methods,” *IEEE Journal of Selected Topics in Signal Processing*, vol. 9, no. 8, pp. 1570–1582, Dec 2015.
- [19] H. Griffiths and C. Baker, “Passive coherent location radar systems. part 1: performance prediction,” *Radar, Sonar and Navigation, IEEE Proceedings -*, vol. 152, no. 3, pp. 153–159, June 2005.
- [20] C. Baker, H. Griffiths, and I. Papoutsis, “Passive coherent location radar systems. part 2: waveform properties,” *Radar, Sonar and Navigation, IEEE Proceedings -*, vol. 152, no. 3, pp. 160–168, June 2005.

- [21] Q. Wu, Y. D. Zhang, M. G. Amin, and B. Himed, “High-resolution passive SAR imaging exploiting structured Bayesian compressive sensing,” *IEEE Journal of Selected Topics in Signal Processing*, vol. 9, no. 8, pp. 1484–1497, Dec 2015.
- [22] D. E. Hack, L. K. Patton, B. Himed, and M. A. Saville, “Detection in passive MIMO radar networks,” *IEEE Transactions on Signal Processing*, vol. 62, no. 11, pp. 2999–3012, June 2014.
- [23] P. Krysik and K. Kulpa, “The use of a GSM-based passive radar for sea target detection,” in *Radar Conference (EuRAD), 2012 9th European*, Oct 2012, pp. 142–145.
- [24] C. Yarman and B. Yazici, “Synthetic aperture hitchhiker imaging,” *IEEE Transactions on Imaging Processing*, pp. 2156–2173, 2008.
- [25] L. Wang, C. Yarman, and B. Yazici, “Doppler-Hitchhiker: A novel passive synthetic aperture radar using ultranarrowband sources of opportunity,” *Geoscience and Remote Sensing, IEEE Transactions on*, vol. 49, no. 10, pp. 3521–3537, Oct 2011.
- [26] L. Wang and B. Yazici, “Passive imaging of moving targets exploiting multiple scattering using sparse distributed apertures,” *Inverse Problems*, vol. 28, no. 12, p. 125009, 2012.
- [27] —, “Ground moving target imaging using ultranarrowband continuous wave synthetic aperture radar,” *Geoscience and Remote Sensing, IEEE Transactions on*, vol. 51, no. 9, pp. 4893–4910, Sept 2013.
- [28] S. Wacks and B. Yazici, “Doppler-dpca and doppler-ati: novel sar modalities for imaging of moving targets using ultra-narrowband waveforms,” *IEEE Transactions on Computational Imaging*, vol. 4, no. 1, pp. 125–136, 2018.
- [29] —, “Passive synthetic aperture hitchhiker imaging of ground moving targets - part 1: Image formation and velocity estimation,” *Image Processing, IEEE Transactions on*, vol. 23, no. 6, pp. 2487–2500, June 2014.
- [30] —, “Passive synthetic aperture hitchhiker imaging of ground moving targets part 2: Performance analysis,” *Image Processing, IEEE Transactions on*, vol. 23, no. 9, pp. 4126–4138, Sept 2014.
- [31] L. Wang and B. Yazici, “Bistatic synthetic aperture radar imaging of moving targets using ultranarrowband continuous waveforms,” *SIAM Journal on Imaging Sciences*, vol. 7, no. 2, pp. 824–866, 2014.
- [32] X. Qu, L. Xie, and W. Tan, “Iterative constrained weighted least squares source localization using tdoa and fdoa measurements,” *IEEE Transactions on Signal Processing*, vol. PP, no. 99, pp. 1–1, 2017.
- [33] S. Gogineni, P. Setlur, M. Rangaswamy, and R. R. Nadakuditi, “Comparison of passive radar detectors with noisy reference signal,” in *2016 IEEE Statistical Signal Processing Workshop (SSP)*, June 2016, pp. 1–5.
- [34] K. Kulpa, P. Samczynski, M. Malanowski, L. Maslikowski, and V. Kubica, “The use of CLEAN processing for passive SAR image creation,” in *Radar Conference (RADAR), 2013 IEEE*, April 2013, pp. 1–6.
- [35] K. Kulpa, “The CLEAN type algorithms for radar signal processing,” in *Microwaves, Radar and Remote Sensing Symposium, 2008. MRRS 2008*, Sept 2008, pp. 152–157.
- [36] B. Feng, T. Wang, C. Liu, C. Chen, and W. Chen, “An effective CLEAN algorithm for interference cancellation and weak target detection in passive radar,” in *Synthetic Aperture Radar (APSAR), 2013 Asia-Pacific Conference on*, Sept 2013, pp. 160–163.
- [37] L. Hongchao, L. Bing, G. Hongqi, and H. Biao, “Reconstruction of reference signal for dvb-s based passive radar systems,” *International Journal of Signal Processing Systems*, vol. 1, no. 1, pp. 116–120, 2013.

- [38] M. K. Baczyk and M. Malanowski, “Decoding and reconstruction of reference DVB-T signal in passive radar systems,” in *11-th INTERNATIONAL RADAR SYMPOSIUM*, June 2010, pp. 1–4.
- [39] W. Xianrong, W. Junfang, H. Sheng, and T. Hui, “Reconstruction of reference signal for dtmb-based passive radar systems,” in *Proceedings of 2011 IEEE CIE International Conference on Radar*, vol. 1, Oct 2011, pp. 165–168.
- [40] O. Mahfoudia, F. Horlin, and X. Neyt, “Optimum reference signal reconstruction for dvb-t based passive radars,” in *2017 IEEE Radar Conference (RadarConf)*, May 2017, pp. 1327–1331.
- [41] M. K. Baczyk and M. Malanowski, “Reconstruction of the reference signal in dvb-t-based passive radar,” *International Journal of Electronics and Telecommunications*, vol. Vol. 57, No. 1, pp. 43–48, 2011.
- [42] K. Gregor and Y. LeCun, “Learning fast approximations of sparse coding,” pp. 399–406, 2010.
- [43] M. Borgerding and P. Schniter, “Onsager-corrected deep learning for sparse linear inverse problems,” *arXiv:1607.05966*, 2016.
- [44] M. Andrychowicz, M. Denil, S. Gomez, M. W. Hoffman, D. Pfau, T. Schaul, and N. de Freitas, “Learning to learn by gradient descent by gradient descent,” in *Advances in Neural Information Processing Systems*, 2016, pp. 3981–3989.
- [45] P. Putzky and M. Welling, “Recurrent inference machines for solving inverse problems,” *arXiv:1706.04008*, 2017.
- [46] B. Yonel, E. Mason, and B. Yazici, “Deep learning for passive synthetic aperture radar,” *IEEE Journal of Selected Topics in Signal Processing*, vol. 12, no. 1, pp. 90–103, 2018.
- [47] H. Leung and S. Haykin, “The complex backpropagation algorithm,” *IEEE Trans. Signal Processing*, vol. 39, no. 9, pp. 2101–2104, 1991.
- [48] B. Yonel, E. Mason, and B. Yazici, “Deep learning for waveform estimation in passive synthetic aperture radar imaging,” in *Algorithms for Synthetic Aperture Radar Imagery XXV*, vol. 10647. International Society for Optics and Photonics, 2018, p. 106470E.
- [49] —, “Deep learning for waveform estimation in passive synthetic aperture radar,” to appear in *Radar Conference (RadarConf) 2018 IEEE Proceedings*.
- [50] E. Mason, B. Yonel, and B. Yazici, “Deep learning for radar,” in *Radar Conference (RadarConf), 2017 IEEE*. IEEE, 2017, pp. 1703–1708.
- [51] K. Hornik, “Approximation capabilities of multilayer feedforward networks,” *Neural Networks*, vol. 4, no. 2, pp. 251 – 257, 1991.
- [52] G. Cybenko, “Approximation by superpositions of a sigmoidal function,” *Mathematics of Control, Signals and Systems*, vol. 2, no. 4, pp. 303–314, 1989.
- [53] G. F. Cooper, “The computational complexity of probabilistic inference using bayesian belief networks,” *Artificial intelligence*, vol. 42, no. 2-3, pp. 393–405, 1990.
- [54] I. Goodfellow, Y. Bengio, and A. Courville, “Deep learning,” 2016, book in preparation for MIT Press. [Online]. Available: <http://www.deeplearningbook.org>
- [55] Y. N. Dauphin, R. Pascanu, C. Gulcehre, K. Cho, S. Ganguli, and Y. Bengio, “Identifying and attacking the saddle point problem in high-dimensional non-convex optimization,” in *Advances in neural information processing systems*, 2014, pp. 2933–2941.
- [56] L. Cimini, “Analysis and simulation of a digital mobile channel using orthogonal frequency division multiplexing,” *IEEE Transactions on Communications*, vol. 33, no. 7, pp. 665–675, Jul 1985.

- [57] H.-S. Chen, W. Gao, and D. G. Daut, "Spectrum sensing for OFDM systems employing pilot tones," *IEEE Transactions on Wireless Communications*, vol. 8, no. 12, 2009.
- [58] Z. Zhao, X. Wan, D. Zhang, and F. Cheng, "An experimental study of HF passive bistatic radar via hybrid sky-surface wave mode," *IEEE Transactions on Antennas and Propagation*, vol. 61, no. 1, pp. 415–424, Jan 2013.
- [59] J. R. G. del Arroyo and J. A. Jackson, "SAR imaging using WiMAX OFDM PHY," in *2011 IEEE RadarCon (RADAR)*, May 2011, pp. 129–134.
- [60] S. Gogineni, M. Rangaswamy, and A. Nehorai, "Passive multistatic radar based on long-term evolution signals," in *2014 48th Asilomar Conference on Signals, Systems and Computers*, Nov 2014, pp. 1413–1417.
- [61] H. A. Harms, L. M. Davis, and J. Palmer, "Understanding the signal structure in DVB-T signals for passive radar detection," in *Radar Conference, 2010 IEEE*. IEEE, 2010, pp. 532–537.
- [62] Q. Wang, C. Hou, and Y. Lu, "An experimental study of WiMAX-based passive radar," *IEEE Transactions on Microwave Theory and Techniques*, vol. 58, no. 12, pp. 3502–3510, 2010.
- [63] C. Yarman, B. Yazici, and M. Cheney, "Bistatic synthetic aperture radar imaging for arbitrary flight trajectories," *Image Processing, IEEE Transactions on*, vol. 17, no. 1, pp. 84–93, Jan 2008.
- [64] P. L. Combettes and V. R. Wajs, "Signal recovery by proximal forward-backward splitting," *Multiscale Modeling & Simulation*, vol. 4, no. 4, pp. 1168–1200, 2005.
- [65] J. T. Rolfe and Y. LeCun, "Discriminative recurrent sparse auto-encoders," *arXiv:1301.3775*, 2013.
- [66] K. Kreutz-Delgado, "The complex gradient operator and the cr-calculus," *arXiv preprint arXiv:0906.4835*, 2009.

A Appendices

A.1 Waveform Derivative

Due to having real valued representations such that $\boldsymbol{\rho}^k \in \mathbb{R}^N$, and $\bar{\boldsymbol{\rho}}^* = \boldsymbol{\rho}^*$ the first component of complex backpropagation equation becomes:

$$\frac{\partial \ell(\mathbf{d}^*, \mathbf{d})}{\partial \boldsymbol{\rho}^*} = \mathbf{F}^T(\bar{\mathbf{d}}^* - \bar{\mathbf{d}}) + \mathbf{F}^H(\mathbf{d}^* - \mathbf{d}) = 2 \operatorname{Re}(\mathbf{F}^H(\mathbf{d}^* - \mathbf{d})) \quad (44)$$

which is purely real valued as expected. From the chain rule with (44) and the normalization derivative $\frac{\partial \boldsymbol{\rho}^*}{\partial \boldsymbol{\rho}^L}$, we obtain the non-layer dependent component of the network derivative in (40):

$$\frac{\partial \boldsymbol{\rho}^*}{\partial \boldsymbol{\rho}^L} \frac{\partial \ell(\mathbf{d}^*, \mathbf{d})}{\partial \boldsymbol{\rho}^*} = \left(-\frac{1}{\|\boldsymbol{\rho}^L\|_\infty^2} \frac{\partial \|\boldsymbol{\rho}^L\|_\infty}{\partial \boldsymbol{\rho}^L} \boldsymbol{\rho}^{LT} + \frac{1}{\|\boldsymbol{\rho}^L\|_\infty} \mathbf{I}_{N \times N} \right) \times 2 \operatorname{Re}\{\mathbf{F}^H(\mathbf{d}^* - \mathbf{d})\} \quad (45)$$

where the partial of the infinity norm of $\boldsymbol{\rho}^L$ is simply a column vector with entry 1 at index of the maximal element of $\boldsymbol{\rho}^L$, and 0's else.

First we consider the second term in the brackets of (40). $\frac{\partial \mathbf{F}}{\partial \mathbf{F}}$ tensor is an $M \times N$ array of $M \times N$ matrices. (m, n) th matrix in the array, \mathbf{I}_{mn} , has all entries $\mathbf{I}_{mn}(i, j) = 0$ except for 1 at $i = m, j = n$. From the definition of the tensor-vector multiplication $\frac{\partial \mathbf{F}}{\partial \mathbf{F}} \boldsymbol{\rho}^* = \sum_{i=1}^M \mathbb{I}_{M \times N \times M} \boldsymbol{\rho}_i^*$ yields an $M \times N \times M$ tensor $\tilde{\mathbf{I}} = [\tilde{\mathbf{I}}_1, \tilde{\mathbf{I}}_2, \dots, \tilde{\mathbf{I}}_M]$ where the m th row of $\tilde{\mathbf{I}}_m$ equals $\boldsymbol{\rho}^{*T}$, 0's otherwise. After another tensor-vector multiplication with conjugate error term, the second expression yields:

$$\left(\frac{\partial \mathbf{F}}{\partial \mathbf{F}} \boldsymbol{\rho}^* \right) (\bar{\mathbf{d}}^* - \bar{\mathbf{d}}) = (\bar{\mathbf{d}}^* - \bar{\mathbf{d}}) \boldsymbol{\rho}^{*T} \quad (46)$$

Taking the first component inside the brackets of equation (40), we denote:

$$\partial_{\mathbf{F}}^k \ell = \sum_{i=1}^L \frac{\partial \rho^k}{\partial \mathbf{F}} \frac{\partial \rho^L}{\partial \rho^k} \frac{\partial \rho^*}{\partial \rho^L} \frac{\partial \ell(\mathbf{d}^*, \mathbf{d})}{\partial \rho^*} \quad (47)$$

For each partial derivative of ρ^L with respect to other representations in the network, we can write the chain rule as $\partial \rho^L / \partial \rho^k = (\partial \rho^{k+1} / \partial \rho^k) (\partial \rho^L / \partial \rho^{k+1})$. Moving down the network beginning from layer L , this derivative can be evaluated by multiplying the $\partial \rho^{k+1} / \partial \rho^k$ term repeatedly for $k = L-1, L-2, \dots, 1$. Denote $\mathbf{y}^k = |\mathbf{z}^k|$ where $\mathbf{z}^k = \mathbf{Q}\rho^{k-1} + \alpha \mathbf{F}^H \mathbf{d}$. The partial of ρ^k with respect to ρ^{k-1} can be evaluated as:

$$\frac{\partial \rho^k}{\partial \rho^{k-1}} = \left(\frac{\partial \mathbf{z}^k}{\partial \rho^{k-1}} \frac{\partial \mathbf{y}^k}{\partial \mathbf{z}^k} + \frac{\partial \bar{\mathbf{z}}^k}{\partial \rho^{k-1}} \frac{\partial \mathbf{y}^k}{\partial \bar{\mathbf{z}}^k} \right) \frac{\partial \rho^k}{\partial \mathbf{y}^k} \quad (48)$$

$\partial \rho^k / \partial \mathbf{y}^k$ is merely the derivative of the thresholding function $\mathcal{P}_{\tau \ell_1}(\cdot)$, which is a diagonal matrix with entries 1 at indexes that $\mathbf{y}_i^k > \tau$, and 0 otherwise. Similarly, $\partial \mathbf{y}^k / \partial \bar{\mathbf{z}}^k$ and $\partial \mathbf{y}^k / \partial \mathbf{z}^k$ yield diagonal matrices with entries, for the i^{th} diagonal term, $\mathbf{z}_i^k / (2|\mathbf{z}_i^k|)$ and $\bar{\mathbf{z}}_i^k / (2|\mathbf{z}_i^k|)$ respectively. Finally, the partial derivatives of $\bar{\mathbf{z}}^k$ and \mathbf{z}^k with respect to ρ^{k-1} yield \mathbf{Q}^H and \mathbf{Q}^T respectively. Since \mathbf{Q} is Hermitian symmetric, we have:

$$\frac{\partial \rho^k}{\partial \rho^{k-1}} = \text{Re} \left(\mathbf{Q} \text{diag} \left(\frac{\mathbf{z}_i^k}{|\mathbf{z}_i^k|} \right) \right) \text{diag}(\mathcal{I}_{\mathbf{y}^k > \tau}) \quad (49)$$

with $\mathcal{I}_{\mathbf{y}^k > \tau}$ denoting the set of indexes i such that $\mathbf{y}_i^k > \tau$. For the \mathbf{F} derivative of the network representations, following the same notation we have that:

$$\frac{\partial \rho^k}{\partial \mathbf{F}} = \left(\frac{\partial \mathbf{z}^k}{\partial \mathbf{F}} \frac{\partial \mathbf{y}^k}{\partial \mathbf{z}^k} + \frac{\partial \bar{\mathbf{z}}^k}{\partial \mathbf{F}} \frac{\partial \mathbf{y}^k}{\partial \bar{\mathbf{z}}^k} \right) \frac{\partial \rho^k}{\partial \mathbf{y}^k}. \quad (50)$$

The first component in the parenthesis vanishes because \mathbf{z}^k only depends on \mathbf{F}^H ⁵. From $\frac{\partial \bar{\mathbf{z}}^k}{\partial \mathbf{F}} = \alpha \frac{\partial (\mathbf{F}^T \bar{\mathbf{d}})}{\partial \mathbf{F}}$, indexing the 3^{rd} dimension of the resulting $M \times N \times N$ tensor with i , at each i , with subscript $:, j$ denoting the j^{th} column we have:

$$\left(\frac{\partial (\mathbf{F}^T \bar{\mathbf{d}})_i}{\partial \mathbf{F}} \right)_{:,j} = \begin{cases} \bar{\mathbf{d}} & \text{if } j = i \\ \mathbf{0} & \text{else} \end{cases}$$

Denoting previous terms computed as $\partial \ell_{\rho^k}$, the \mathbf{F} -derivative at the layer k becomes:

$$(\partial_{\mathbf{F}}^k \ell)_{:,i} = \frac{\alpha (\partial \ell_{\rho^k})_i}{2} \frac{(\mathbf{Q}\rho^k + \alpha \mathbf{F}^H \mathbf{d})_i}{|(\mathbf{Q}\rho^k + \alpha \mathbf{F}^H \mathbf{d})_i|} \bar{\mathbf{d}} \quad (51)$$

if $|(\mathbf{Q}\rho^k + \alpha \mathbf{F}^H \mathbf{d})_i| = \mathbf{y}_i^k > \tau$ and 0 everywhere else.

Finally, multiplying with the partial derivative of $\mathbf{F} = \text{diag}(\mathbf{w})\tilde{\mathbf{F}}$, we obtain the derivative with respect to \mathbf{w} by, for index $i = 1, 2, \dots, M$, and subscript $i, :$ denoting i^{th} $1 \times N$ row of the corresponding matrix:

$$\left(\frac{\partial \ell}{\partial \mathbf{w}} \right)_i = \tilde{\mathbf{F}}_{i,:} \left(\frac{\partial \ell}{\partial \mathbf{F}} \right)_{i,:} \quad (52)$$

A.2 Threshold Derivative

Since all inputs to activation function are positive $\rho_i^k = \max(0, \mathbf{y}_i^k - \tau)$, the derivative $(\partial \rho^k / \partial \tau)_{1 \times N}$ will equal -1 at indexes $\mathbf{y}_i^k > \tau$ and 0 otherwise. Then the from k^{th} layer derivative becomes:

$$\frac{\partial \ell}{\partial \tau} = \sum_{k=1}^L \sum_{i \in \mathcal{I}_{\mathbf{y}^k > \tau}} - \left(\frac{\partial \rho^L}{\partial \rho^k} \frac{\partial \rho^*}{\partial \rho^L} \frac{\partial \ell(\mathbf{d}^*, \mathbf{d})}{\partial \rho^*} \right)_i \quad (53)$$

where $\mathcal{I}_{\mathbf{y}^k > \tau}$ is again the set of indexes where $\mathbf{y}^k = |\mathbf{Q}_i \rho^k + \alpha \mathbf{F}_i^H \mathbf{d}| > \tau$.

⁵This results from the property of Wirtinger derivatives, such that $\frac{\partial \bar{c}}{\partial c} = 0$, for a complex variable $c \in \mathbb{C}$.